Short Term Mobility Program 2016

Short Term Visit of Prof. Mark S. Kulie
Michigan Technological University, Houghton, MI, USA
at CNR/ISAC- Roma

28 May-13 June 2017

Final Report

Investigating the Ice Scattering Signature of the Global Precipitation Measurement (GPM) Microwave Imager's (GMI) High Frequency Channels Under Varying Precipitation Conditions

Dott.ssa Giulia Panegrossi

CNR-ISAC Sede secondaria di Roma
Area della Ricerca di Tor Vergata
Via del Fosso del Cavaliere 100
00133 Roma
email: g.panegrossi@isac.cnr.it

Rome, 22 June 2017

1. Objectives:

Prof. Mark Kulie has been collaborating with our group at CNR-ISAC in Rome since 2015. One of the main purposes of our collaboration is to establish the potential and limitations of passive microwave spaceborne observations available from the most advanced radiometers in the Global Precipitation Measurement (GPM) constellation to detect snowfall. Prof. Kulie's expertise in snowfall retrieval and analysis using passive and active spaceborne microwave observations, combined with the expertise of the satellite meteorology group at CNR-ISAC (Rome branch) in passive microwave retrieval of precipitation, serve as the foundation of our collaboration and of Dr. Kulie's work during his visit within the Short Term Mobility program 2016.

The work of Prof. Kulie during his visit at CNR-ISAC (Rome) has focused on three main objectives:

1) Research on the state-of-the-art on the use of spaceborne passive microwave measurements for snowfall detection;

2) Analysis of case studies to investigate on the limitations and capabilities of the Global Precipitation Measurement (GPM) Microwave Imager (GMI) (the most advanced spaceborne microwave radiometer currently available) to observe snowfall at higher latitudes using coincident spaceborne snowfall estimates available from the CloudSat Cloud Profiling Radar (CPR);

3) Use of a global GMI/CPR coincidence dataset to analyze GMI high frequency signatures and CPR snowfall observations in relation to key environmental characteristics (i.e., background surface and integrated water vapor content).

2. State-of-the-art on the use of spaceborne passive microwave measurements for snowfall detection

Snowfall detection from space using passive microwave observations is extremely challenging. Two main obstacles are encountered by passive microwave snowfall retrieval schemes: the inability to reliably distinguish the respective falling snow and background surface contributions to the upwelling radiation from the earth/atmosphere system (e.g., Skofronick-Jackson and Johnson 2011; You et al. 2016) and quantitative precipitation estimation uncertainties related to varying and ill-constrained ice/snow microphysical properties that obfuscate high microwave frequency ice/snow particle scattering signatures (e.g., Kulie et al. 2010). High latitude surfaces are also frequently (or permanently) snow or ice-covered with elevated and variable surface emissivities (Prigent et al. 2006; Turk et al. 2014), thus rendering the solid precipitation contribution to upwelling microwave radiation difficult to isolate from the surface contribution. This issue is further magnified by the relatively subtle passive microwave signal associated with low precipitation rates (Kongoli et al. 2015). Various studies have shown that extremely light snowfall rates dominate the snowfall rate distribution at higher latitudes (Liu 2008; Kulie and Bennartz 2009; Kulie et al. 2016).

Microwave sensors with high frequency channel diversity offer the best opportunity for significant advances in surface snowfall retrievals. The lengthy legacy microwave radiometer imager precipitation data record collected by such instruments as the Special Sensor Microwave Imager (SSM/I), the Tropical Rainfall Measuring Mission (TRMM) Microwave Imager (TMI), and the Advanced Microwave Scanning Radiometer-EOS (AMSR-E) included microwave channels up to 85/89 GHz. While the 85/89 GHz channels are considered high frequency microwave channels with demonstrated ice scattering sensitivity associated with tropical and mid-latitude rain events (e.g., Spencer et al, 1989; Bennartz and Petty 2001). The 85/89 GHz channels on microwave imagers

that employ fixed oblique observation angles can be especially useful for oceanic precipitation rate retrievals by exploiting high frequency polarization signals. Against the highly polarized oceanic background under clear sky conditions with decreasing polarization trends under opaque cloudy and precipitating scenes, tools that exploit polarization information (e.g., the Petty (1994) scattering index) have been developed to isolate the ice scattering TB signature at higher microwave frequencies. The 85/89 GHz channel, however, is too sensitive to the surface for consistently effective higher latitude snowfall remote sensing over land surfaces (Skofronick-Jackson and Johnson 2011). Higher frequency "window" channels located in 150-170 GHz range, combined with observations utilizing gaseous absorption features between 100-200 GHz, can be exploited for snowfall detection since they respond more effectively to ice microphysics compared to 85/89 GHz channels (e.g., Liu 2008; Kulie et al. 2010; Kuo et al 2016; Olson et al. 2016). More importantly, these higher frequency channels – including the so-called "window" channels - are less prone to surface effects due to their sensitivity to water vapor or oxygen absorption (Skofronick-Jackson et al. 2004). Current microwave imagers such as the Global Precipitation Measurement (GPM) Microwave Imager (GMI), combination microwave imager/sounders (e.g., Special Sensor Microwave Imager and Sounder (SSMIS)), and microwave sounders (e.g., Advanced Technology Microwave Sounder (ATMS)) offer such channel combinations that can be used for snowfall detection and quantitative precipitation retrievals.

Theoretical modeling studies have been carried out to demonstrate the potential of high frequency channel combinations for snowfall detection purposes (e.g., Bennartz and Bauer 2003; Di Michele and Bauer 2006). Oceanic snowfall rate estimation using high frequency channels should hypothetically be a more tractable retrieval scenario due to a fairly well-behaved and understood surface background. Skofronick-Jackson and Johnson (2011), however, indicate complexities over land surfaces by quantifying the contribution to the top-of-the-atmosphere modeled brightness temperatures (TB) at multiple frequencies exceeding 89 GHz under different snowfall regimes. The 89 GHz channel contained a significantly larger fraction of the TB signal derived from an assumed mixed forested surface for all snowfall events compared to higher frequencies. Higher frequencies (e.g., 166 and 183.3 GHz channels) were more sensitive to frozen hydrometeor scattering and partially masked the surface contribution, but with varying degrees of sensitivity depending on the ice water path and atmospheric moisture profile associated with each snowfall regime. The Skofronick-Jackson and Johnson (2011) results highlight the difficulties associated with isolating the snowfall signal at higher microwave frequencies due to complex interaction between surface and atmospheric features that determine the multi-frequency TB signal.

The application of high frequency channels using 150 and 183.3 GHz microwave sounder channels – more specifically, using TB differences from channel pairs with weighting functions that peak at different atmospheric levels - has also been shown in proof-of-concept snowfall detection studies and snowfall product development (Kongoli et al. 2003; Surussavadee and Staelin 2009; Noh et al. 2009; Kongoli et al. 2015). Noh et al. (2009) illustrate United States Laurentian Great Lakes snowfall retrieval potential using previous generation operational microwave sounder data from the Advanced Microwave Sounding Unit (AMSU-B). They noted generally positive results, especially in the early winter season when sustained ground snow cover is limited. In later winter months, however, snowfall retrievals using sounding channels were susceptible to surface effects via increased false alarm rates (i.e., snow-covered ground displayed a similar differential TB signature as falling snow events). Enhanced screening methods that account for seasonal surface differences can significantly improve false detections (Kongoli et al. 2015).

High frequency microwave channels and surface effects are important factors to consider for the current flagship GPM spaceborne mission. The Goddard Profiling algorithm (GPROF) used for GMI precipitation retrievals recognizes the complications associated with distinctive surface

emissivities associated with different surface types (Kummerow et al. 2015). For a given GMI observation, the GPROF retrieval scheme restricts its *a priori* database search whereby the observation TB vector is optimally matched to a database TB member that minimizes the multi-frequency TB difference. This *a priori* database search restriction is limited to similar surface classes and environments (e.g., 2 m temperature and total precipitable water) as the GMI observation, thus reducing computational time and constraining retrieval possibilities to consider only similar surface types. GPROF snowfall retrieval efficacy is still largely unknown and remains an active research topic, but studies that systematically assess the information content contained in various GMI channel combinations for snowfall detection have been undertaken in recent years using spaceborne radar observations to identify snow events globally. For instance, You et al. (2016) analyzed a coincident GMI and GPM Dual-frequency Precipitation Radar (DPR) database to determine optimal channel combinations for snowfall detection over land. Low frequency channels obviously demonstrate little information due to a weak ice scattering response. Including high frequency channels near the 183.3 GHz water vapor absorption line were deemed valuable, but adding the 166 GHz channel to a multi-frequency channel combination is deemed optimal for snowfall detection a GMI-like sensor. The 166 GHz channel amplifies ice/snow scattering sensitivity lower in the atmosphere, yet appropriately dampens surface influences and increases snowfall detection statistics when compared to radar-derived snow/no-snow statistics.

Compiling and exploiting other coincident spaceborne active and passive microwave sensor datasets will further enhance our understanding of high frequency microwave snowfall detection capabilities. CloudSat's sensitive Cloud Profiling Radar (CPR) has proved extremely valuable for global snowfall research (e.g., Liu 2008; Kulie et al. 2009; Boening et al. 2012; Behrangi et al. 2016; Kulie et al 2016). Combined radiometer (GMI, AMSR-E, SSMIS) and CloudSat observations can be exploited to study radiometric signals associated with a broader range of the snowfall rate spectrum compared to the GPM DPR since the effective ~12 dBZ GPM DPR sensitivity threshold limits its effectiveness to detect lighter snow events (Casella et al. 2017). This report illustrates case study analyses from a matched GMI/CPR dataset that provides instructive insights to highlight widely varying GMI multi-frequency signals associated with different snowfall types (Section 3). The case study results are followed by an aggregated brightness temperature response analysis of the entire GMI/CPR dataset to show GMI snowfall detection efficacy over different surface types associated as a function of ambient atmospheric water vapor content (Section 4). High frequency microwave brightness temperatures associated with surface snowfall events are also investigated over the North Atlantic Ocean to study possible systematic scattering differences linked with snowfall modes (Section 5). All of these components will ultimately improve our ability to interpret GMI observations and study GMI snowfall retrieval strengths and shortcomings when merged with GPROF retrievals in following studies.

3. Case study analysis

Three main case studies that are part of the combined GMI/CPR snowfall dataset have been identified and analyzed during Prof. Kulie's visit. Two case studies that describes an intense, widespread frontal snowfall event and a frontal rain to snow transition event are included in this report for illustrative purposes. Other interesting snowfall events (e.g., orographic snow, convective snow, snow over ice surfaces, etc.) will be compiled and analyzed in a similar fashion. These analyses are believed to be the first exhaustive GMI TB analyses of varied snowfall events, using CloudSat CPR and CALIPSO lidar products to augment the GMI observations.

3.1 Intense snowfall event on 30 April 2014.

This widespread frontal snowfall event occurred over Eastern Russia north of the Sea of Okhotsk. The more sensitive CPR indicated maximum cloud top heights between ~5-8 km from ~58.5-61° latitude. Typical maximum radar reflectivity values were between 10-15 dBZ, with some embedded regions exceeding these values. The CPR also observes shallower cloud structures with cloud top heights less than ~2 km capable of producing snow north of 61° latitude. CPR reflectivity values associated with the shallower snowfall are consistently weaker than the deeper snowfall located further south.
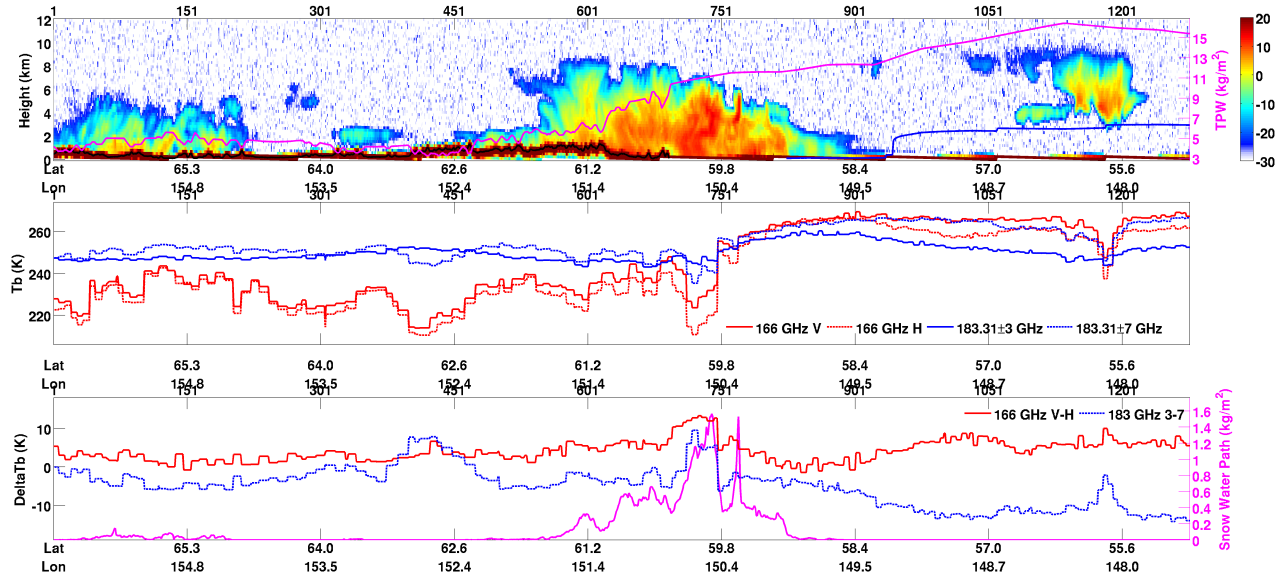

Fig. 1a: Snowfall event on 30 April 2014. Top panel CPR reflectivity (colorbar) and the TPW (in pink), and freezing level height (in blue). Middle panel: TBs at 166 GHz (V and H polarization, in red), and 183.3±3 GHz and 183.3±8 GHz (in blue). Bottom panel: TB difference (ΔTB) at 166 GHz (V-H, in red), and for the two channels at 183.3 GHz (in blue), along with the snow water path (SWP) as estimated in the CPR 2C-SNOW product.
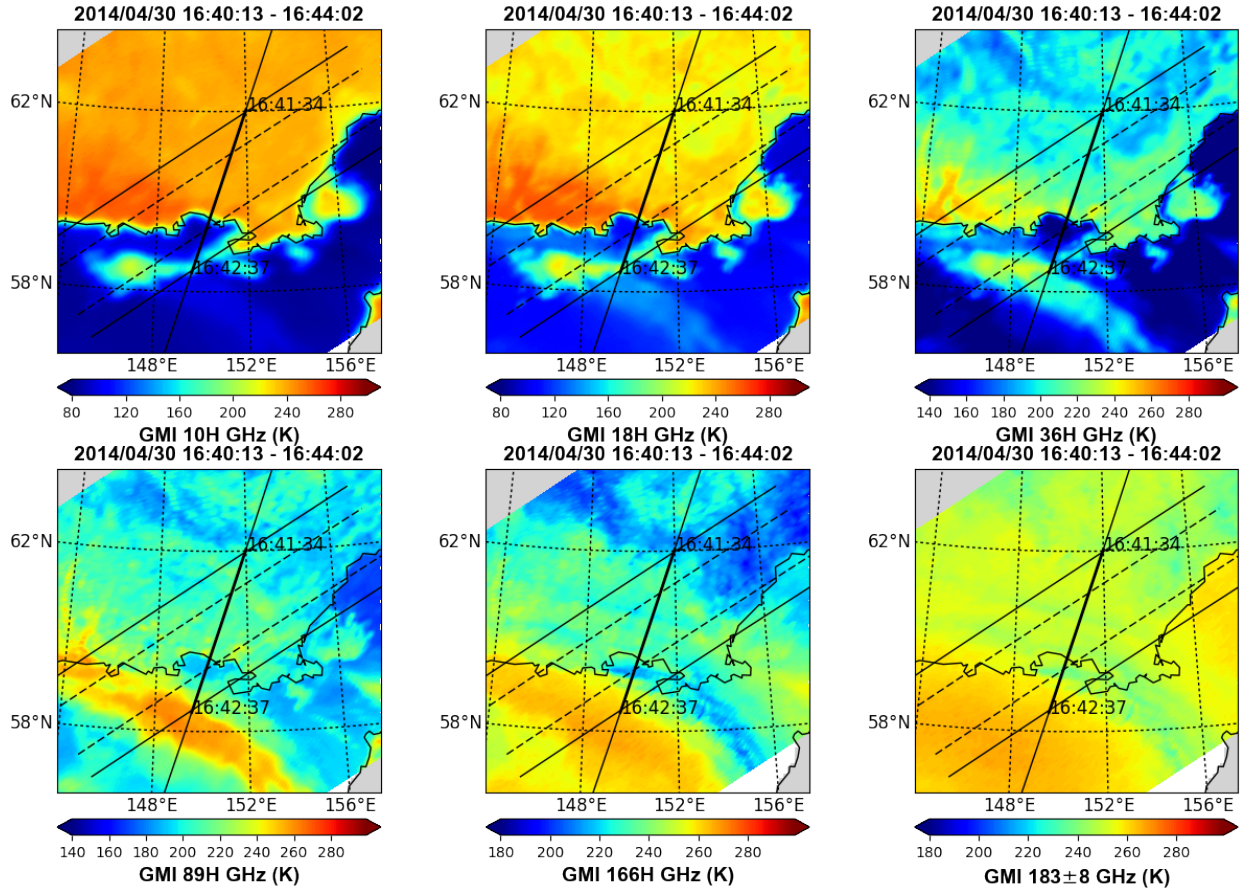
Fig. 1b: Snowfall event on 30 April 2014. Maps of GMI TBs (H-pol) at 10 GHz, 18.7 GHz, 36 GHz, 89 GHz, 166 GHz, and 183±8 GHz.

This case exhibits a land to ocean transition, with extremely dry total precipitable water (TPW) values near ~2 mm in the north sector of the scene increasing to over 15 mm in the southern sector (Fig. 1a, top panel). A particularly significant TPW change is observed south of 59°N, presumably indicating a distinct frontal structure. Land surfaces are very likely snow covered at this latitude.

In Casella et al. (2017), the DPR Ku uncorrected reflectivity profiles reveal that most of the event north of 60° latitude and at higher altitudes is missed by the DPR due to the degraded radar sensitivity compared to the CPR. Casella et al. (2017) show that DPR Ku uncorrected reflectivity displays some structure below ~4 km in the deeper snowfall segment of this event between ~58.8-60° latitude. In the deeper snowfall segments, 166 GHz and 183+-7 GHz TBs show some sensitivity with decreasing TBs (i.e., ~15-20 K decrease in 166 GHz TBs) due to the scattering effect of columnar ice content. In this segment, the 166 GHz (V-H) TB differences (ΔTB) also show an increase in the polarization corresponding to the deeper and most intense clouds. This 166 (V-H) GHz feature is correlated to the 183 GHz ΔTB increase.

In correspondence of the shallower/weaker snow clouds (north of 60°N), 166 GHz TBs *increase* with respect to the background: this is the effect of the presence of cloud supercooled droplets. 166 GHz TBs typically decrease due to scattering by sufficient columnar ice content, but this case highlights the sensitivity of 166 GHz to supercooled cloud liquid water. The presence of supercooled water near cloud tops in these shallow clouds has been verified using the CloudSat CPR/CALIPSO DARDAR product (not shown, http://www.icare.univ-lille1.fr/projects/dardar).

6

Moving south from 58.4 °N 166 GHz and 183 GHz TBs progressively increase due the atmospheric water vapor gradient (increasing south of 59°N). Atmospheric temperatures also increase further south (note the abrupt freezing level height increase around 57°N). This effect dampens the scattering effect due to the shallow and weaker portion of the clouds south of 58.4°N. The high frequency channels show sensitivity to the deep cloud with reflectivity exceeding 10 dBZ above 5 km, or in correspondence of the upper level cloud at 55.6°N. South of 58.4°N and between 148-152°E, where CPR shows lower reflectivity values (< 0 dBZ) and shallow surface snowfall structures (according the 2C-SNOW product), GMI TBs show higher values at lower frequencies (< 37 GHz, see Fig. 1b) with respect to the "cold" surrounding water surface, thus indicating the presence of melting snow/liquid water at very low levels. This feature is also clearly evident in the GMI TB maps in Fig. 1b, including faint signatures at the lowest frequencies (10 and 18 GHz). At high frequencies (166GHz and above) there is no evidence of such structure because of the dampening effect of the water vapor (weighting functions peaking at higher levels with respect to the shallow cloud). Even the emission due to supercooled cloud liquid water droplets in the upper cloud layers (as evidenced by the DARDAR CloudSat CPR/CALIPSO product) is not visible at 166 GHz in this region because of the high TPW values. At low frequencies, the emission signal is more evident north of 58°N and west of 148°E (very likely associated with rainfall) and it is much less evident east of 148°E, where it is likely associated to melting snow or drizzle, and where the emission by supercooled droplets is evident at 89 GHz.

3.2 Frontal precipitation (rainfall/snowfall) event on 12 April 2014.

The second case study over interior Alaska on 12 April 2014 is a frontal stratiform snowfall event exhibiting an extensive geographic footprint, transitioning to rainfall south of 61.3°N. The CPR observations indicate cloud top heights ranging from ~6-8 km and maximum near surface W-band radar reflectivities exceeding 10 dBZ and approaching 20 dBZ.
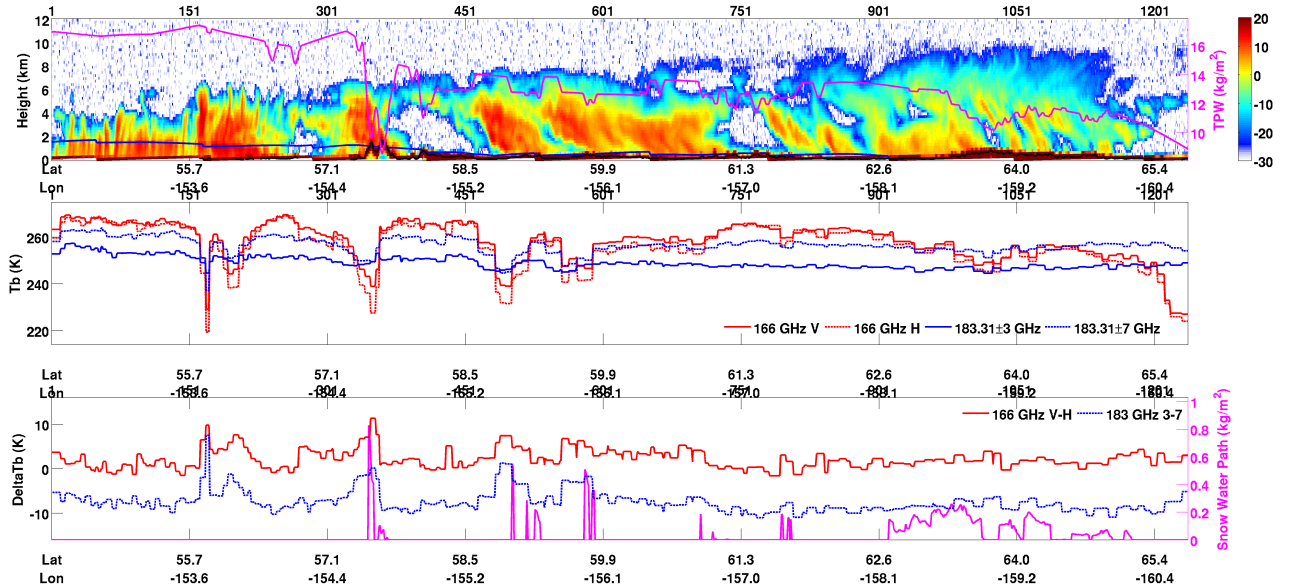

Fig. 2: Same as in Fig. 1 but for rainfall and snowfall event on 12 April 2014.

This case shows a transition from ocean to land going from south to north. Unlike the previous case, there is not significant TPW variability at the upper levels since the 183+/-3 GHz TBs are nearly invariant across the entire domain; the decrease in TPW north of 64°N is probably die to lower level dry air intrusions not sensed by the 183+/-3 GHz channel.

CPR indicates likely surface precipitation over almost entire domain. CPR, however, classifies surface precipitation as rain south of ~62°N where ECMWF indicated freezing levels are elevated above ground level (T_{2m} > 0°C), except a few locations associated with mountains/hills where precipitation is classified as snow. CPR indicated snowfall occurs north of 62°N where T_{2m} < 0°C. Columnar ice values from the 2C-SNOW product are evident mostly over the ocean (note that 2C-SNOW produces snow water content profiles only where the product indicates possible surface snow or if estimated liquid fraction is < 0.1). Columnar ice over land is associated with the deep cloud structures south of 62°N – again, 2C-SNOW only retrieves ice content profiles where surface snow occurs. Most of the rain with fairly low freezing levels contains ice above the freezing level (as seen in the reflectivity profiles).

166 GHz and 183+-7 GHz TBs show sensitivity to the presence of ice/snow mostly corresponding to the deepest cloud structures (57.1°N, 58°N, 59.9°N) with high reflectivity(> 10-15 dBZ) at higher levels (around 4-5 km height). Most of these deep cloud structures are associated with surface rainfall. In the snowfall sector north of 62°N, 166 GHz and 183+-7 GHz TBs are less sensitive to the deeper (up to 8 km) and more intense cloud structures, although reflectivities are generally < 10 dBZ in the surface snow locations. In the snowing regions, 89 GHz TBs are affected by snow-covered surfaces due to lower TPW values, while TBs at 166 GHz are much less affected by the surface (only starting at 66°N where TPW is significantly reduced) – the effective 166 GHz water vapor mask enables snowfall detection throughout most of this region. TBs at 166 GHz and above are also not significantly affected by the cloud. CALIPSO reveals the presence of a thick layer of small ice particles (small effective radius) compared to the deep clouds in the rainfall sector. Moreover, CALIPSO does not show presence of supercooled droplets embedded in this cloud, so the lack of scattering signal at 166 GHz and above is due to the fact that the ice crystals are small (very likely). However, the slight increase of 166 GHz TBs at 62°N is related to the presence of supercooled droplets (revealed by CALIPSO), again illustrating the sometimes extreme sensitivity to cloud liquid water at this frequency.

The light snowfall in this case, even if associated with relatively deep cloud structures, may not display obvious high frequency scattering signatures. ΔTB, however, increases in correspondence of the deeper and more intense cloud structures south of 62°N, while there is much lower variability in correspondance of the snowfall structure associated to the snowfall north of 62°N. The lack of ΔTB signal for the snowfall cloud is probably due to updrafts and upper level dynamics generating the tilted structure visible in the CPR cross section. ΔTB variability at 166 GHz (V-H) is correlated to ΔTB at 183 GHz but it shows a larger variability than at 183 GHz. This feature is very important because it shows the potential of 166 GHz ΔTB for snowfall detection.

4. Analysis of a global GMI/CPR coincidence dataset

Different background types are identified using a surface classification algorithm presented in Panegrossi et al. (2017). The response of GMI high frequency channel combinations to the presence of snowfall is analyzed using coincident CloudSat snowfall retrievals (2C-SNOW product) as a reference snowfall dataset.
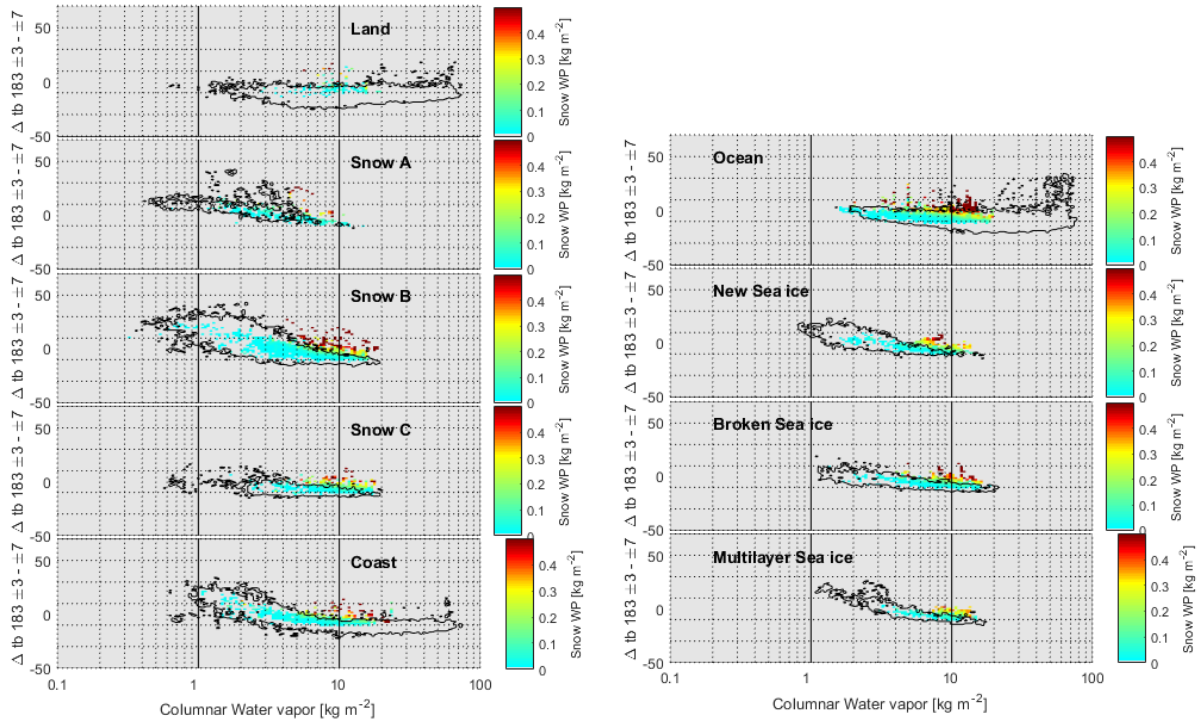
Fig. 4: Scatterplots showing the ΔTB183 vs. TPW for all the points in the GMI/CPR coincident dataset and for different surface types. Color scale indicates the snow water path as estimated by CloudSat CPR (2C_SNOW product), associated to each point in the dataset with snowfall rate at the surface > 0 mm/h (in 2C-SNOW product snow water path is computed when according to the 2C-PRECIP product the snowfall rate at the surface is probable or certain, or if mixed liquid fraction is < 0.1, therefore where CPR snowfall rate at the surface > 0 mm/h). The black contour delineates the manifold for points in the dataset associated to clear sky (i.e., no cloud according to the 2B-CLDCLASS product).

Figure 4 shows ΔTB183 values as a function of TPW, with the clear sky manifold indicated by the black contour line (where clear sky is indicated by the 2B-CLDCLASS product). CloudSat derived snow water paths (SWP) are also indicated by the color table. Figure 4 indicates that snowfall is associated with a wide range of TPW values (1 kg/m^2 < TPW < 20 kg/m^2) over most surfaces, except for snow A where the maximum TPW is limited to ~10 kg/m^2 (i.e., very dry and cold conditions). Peaks of SWP occur where 5 kg/m^2 < TPW < 20 kg/m^2. Figure 4 clearly indicates that in order to analyze the behavior of ΔTB183 versus SWP, it is necessary to know both TPW and surface type.

For TPW > 5 kg/m^2, as SWP increases ΔTB183 increases with respect to its clear sky values. Over most surfaces this happens for SWP larger than 0.2 kg/m^2, and distinct ΔTB183 signals with respect to clear sky are only observed in this case. The potential to truly detect snowfall events using the ΔTB183 metric is therefore limited to the 0.2 kg/m^2 threshold.

The various surface types sometimes display different trends. There are unfortunately very few cases of snowfall over land, or SNOW A, and the majority of events are associated with low SWP. Conversely, there there are *many* cases over ocean (open water) associated with large SWP exceeding 0.5 kg/m^2. Interestingly, we will see in Fig. 6 that the largest SWP is associated to lowest snowfall probability, and lowest SWP to largest probability. There is also a very distinct signal of ΔTB183 increase with SWP over broken ice and new sea ice. Lower SWP is associated to multilayer ice, and therefore the ΔTB183 signal is weaker. The largest SWP among all land surfaces are associated with the Snow B category. Correspondingly, there is a distinct signal of ΔTB183 over Snow B, and also Snow C, surfaces.

9

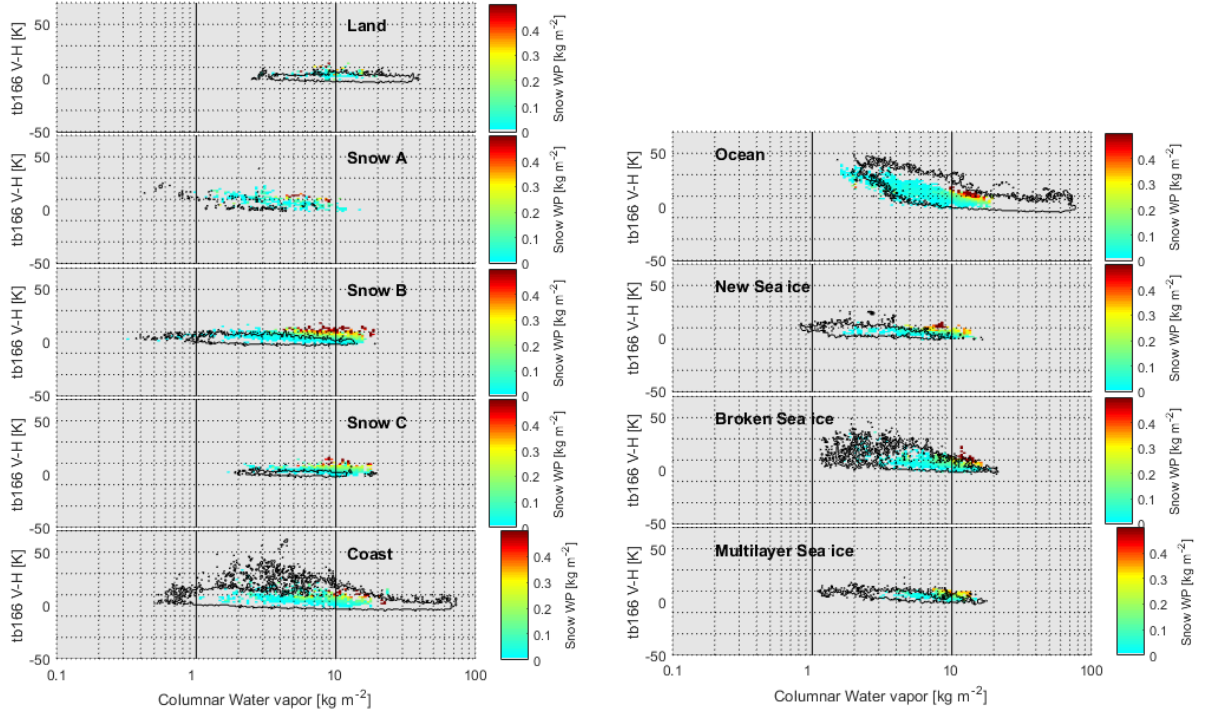**Fig. 5**: Scatterplots showing the ΔTB166 vs. TPW for all the points in the GMI/CPR coincident dataset and for different surface types. Color scale indicates the snow water path as estimated by CloudSat CPR (2C_SNOW product), associated to each point in the dataset with snowfall rate at the surface > 0 mm/h (in 2C-SNOW product snow water path is computed when according to the 2C-PRECIP product the snowfall rate at the surface is probable or certain, or if mixed liquid fraction is < 0.1, therefore where CPR snowfall rate at the surface > 0 mm/h). The black contour delineates the manifold for points in the dataset associated to clear sky (i.e., no cloud according to the 2C-CLASS product).

Fig. 5 shows similar results as Fig. 4, but for ΔTB166 (the 166 GHz V-H difference). Similar to Fig. 4, snowfall is associated to 1 kg/m^2 < TPW < 20 kg/m^2 over most surfaces (except for snow A where max TPW is 10 kg/m^2, i.e., very dry and cold conditions). Peaks of SWP occur where 5 kg/m^2 < TPW < 20 kg/m^2. In order to analyze the behavior of ΔTB166 vs. SWP, it is again necessary to know TPW and surface type.

Over most surfaces (except for land, ocean, and Snow A) and for TPW > 5 kg/m^2, as SWP increases ΔTB166 increases with respect to the corresponding values in clear sky. This happens for SWP larger than 0.2 kg/m^2, only in this case we distinguish a distinct signal of ΔTB166 with respect to clear sky. For Snow C and to a less extent for Snow B for TPW > 12 Kg/m^2, we have a distinct snowfall signal also for very low SWP. Again, there are very few cases of snowfall over land, or SNOW A, and they associated with very low SWP values. Over ocean in clear sky we observe large ΔTB166 for low TPW because the TBs are affected by the surface, and ΔTB166 decreases as TPW increases. Over ocean cases associated with large SWP values do not show a distinct signal compared to clear sky (in fact, Fig. 6 will show low probability of snowfall for these cases). However, we have distinct snowfall occurrence for very low TPW and relatively large ΔTB166. These cases are probably indirectly affected by supercooled droplets lowering ΔTB166 values through the depolarization of the signal from the surface. Fig. 6 will show that these cases are associated with very large snowfall probability. Finally, there is a very distinct ΔTB166 increase signal with SWP over broken ice and new sea ice for SWP > 0.2 kg/m^2. Lower SWP values are associated with multilayer ice, therefore the ΔTB166 signal is weaker.

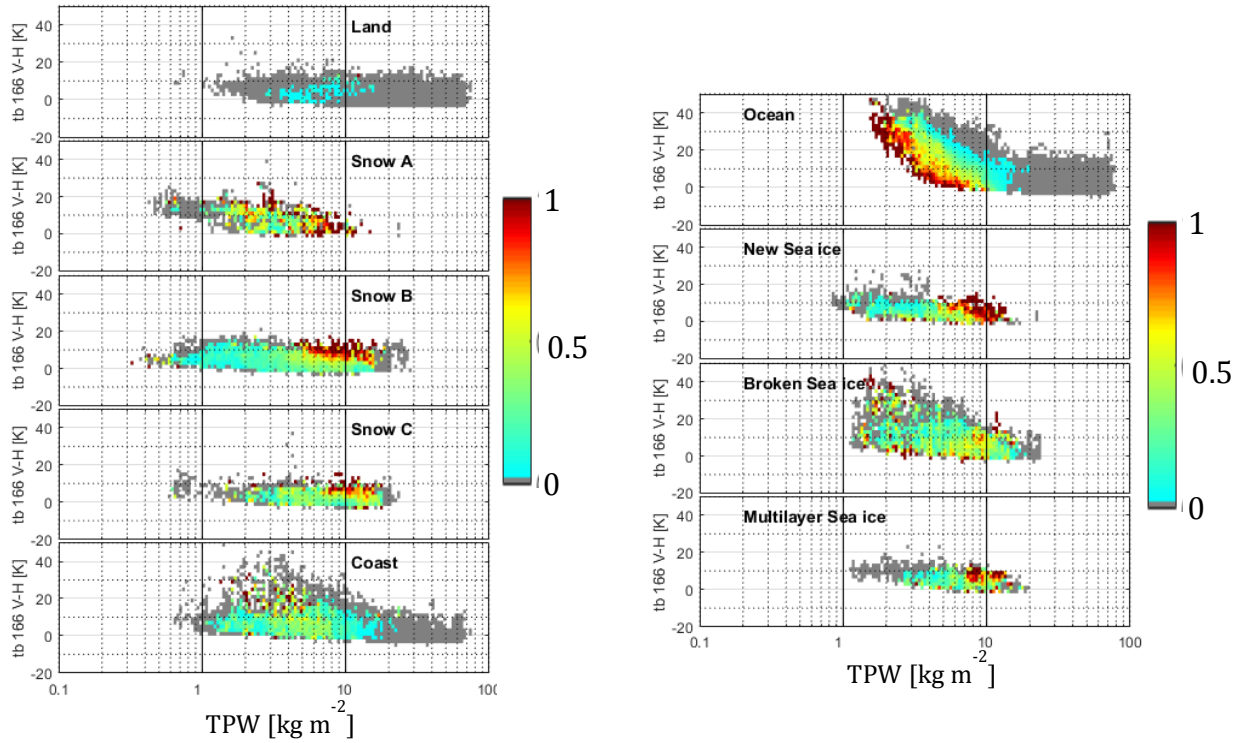**Fig. 6:** Scatterplots showing snowfall probability distribution for all ΔTB166/TPW 2-D bins in the GMI/CPR coincident dataset and for different surface types. Color scale indicates snowfall probability computed for each ΔTB166/TPW 2-D bin (see text for details).

Fig. 6 indicates the snowfall probability distribution for each ΔTB166/TPW bin. For each surface type, for a given combination (bin) of ΔTB166/TPW (or ΔTB183/TPW), snowfall probability is calculated as Ns/(Ns+N0) where Ns is number of occurrences of CPR 2C-SNOW surface snowfall rate > 0 mm/h, N0 occurrences without CPR 2C-SNOW surface snowfall. Over SnowB, Snow C and New Sea Ice, snowfall probability is larger when TPW > 5 kg/m^2. The largest probabilities are associated with larger ΔTB166 for Snow B and Snow C. Over Snow A, there is not a definite trend with TPW or ΔTB166. For New Sea Ice, large snowfall probabilities are associated with 0 K < ΔTB166 < 10 K. Over Snow A and Broken Ice surface, there is not a definite snowfall probability trend with TPW or ΔTB166. Over Multilayer Sea Ice, larger probabilities occur for TPW > 8 kg/m^2. In these cases, higher probabilities are associated with higher ΔTB166 (around 10 K). Over Ocean, the largest probability occurs for TPW < 8 kg/m^2, also for very low TPW (2 kg/m^2) associated with very low SWP (see Fig. 7). There is large ΔTB166 variability (from 0 to 40 K) over ocean, associated with high snowfall probability. Over ocean for a given value of TPW, ΔTB166 decreases as probability increases (depolarization effects). The high probability related to low SWP (see Fig. 8) may be related to indirect effects that alter TBs (e.g., supercooled droplets in mixed phase clouds). Overall, Fig. 6 provides extremely valuable guidance to the microwave remote sensing community regarding the potential of 166 GHz channel information to detect snowfall over various surface types.

5. North Atlantic Ocean snowfall analysis

A final project was launched during Prof. Kulie's recent visit. This project was partially inspired by the analyses shown in Sections 3 and 4, combined with previous work published in Kulie et al. (2016). Kulie et al. (2016) results indicated prominent regions in the North Atlantic Ocean where shallow convective snow comprised a significant amount of snowfall (both from a frequency of occurrence and annual accumulation perspective). Fig. 7 shows a convective snowfall case study using combined CloudSat and AMSR-E observations and products. While the CloudSat

reflectivity swath indicates shallow, yet intense, convective snow structures, AMSR-E precipitation retrievals (based on earlier GPROF versions) did not estimate any precipitation in the region. We
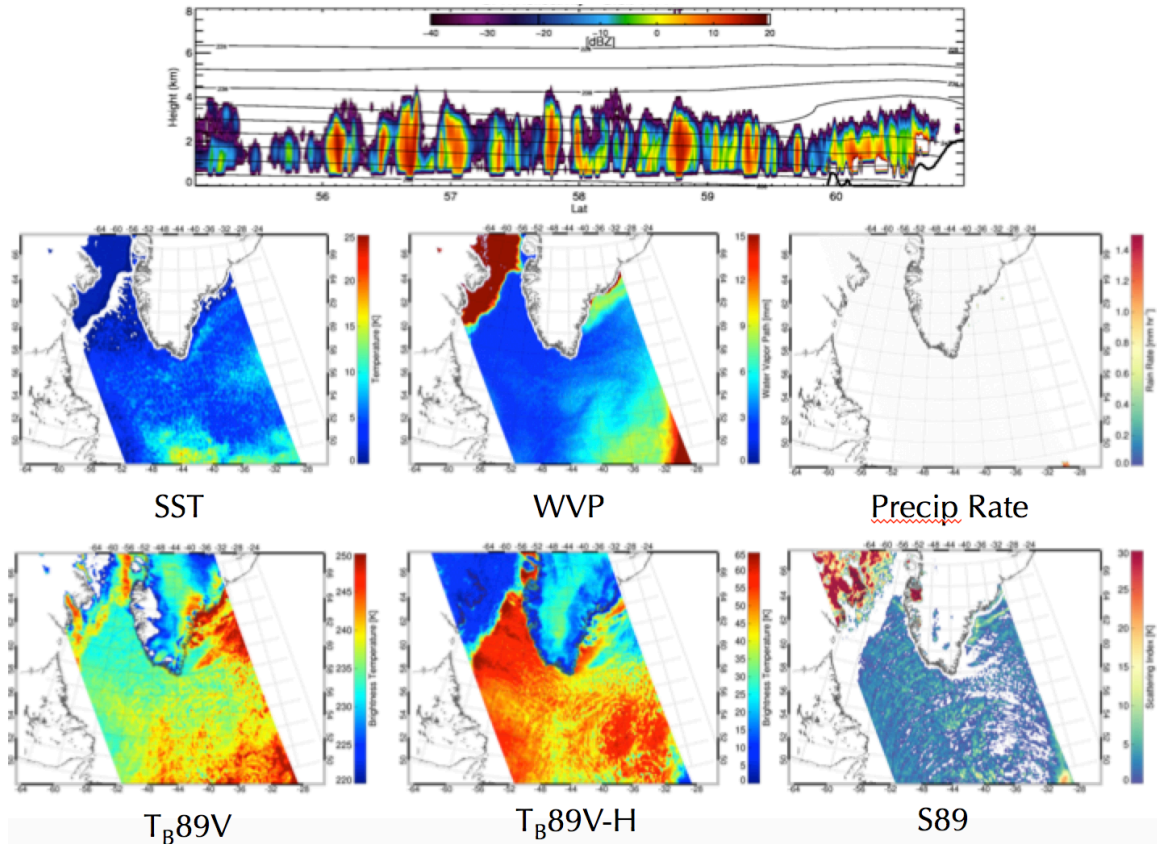

Fig. 7: CloudSat CPR reflectivity profile (top panel) and AMSR-E derived sea surface temperature (SST), water vapor path retrievals (WVP), surface precipitation rate retrievals (Precip Rate), 89 GHz vertically polarized TB (TB89V), 89 V-H TB (TB89V-H), and 89 GHz scattering index (S89) for a convective snowfall event in the North Atlantic Ocean.

have analyzed numerous other convective snow cases using AMSR-E and GMI observations and found similar results – microwave radiometer retrievals struggle to realistically represent surface snowfall rate for typical convective snow events. This particular snowfall mode is unique since it typically occurs in postfrontal environments characterized by extremely low TPW values (extremely dry Arctic air), where the convective snow is forced by turbulent fluxes induced by ocean-air interactions (e.g., extreme low-level instability created by cold air flowing over relatively warm unfrozen large bodies of water). Initial results using an extensive AMRE-E/CloudSat dataset indicate that the 89 GHz scattering signature associated with convective snow is not well correlated with surface snowfall rate (e.g,. no discernable 89 GHz increased scattering signal with increasing surface snowfall rates), but 89 GHz scattering is better correlated with surface snowfall rates for deeper stratiform snowfall events (not shown). Future work will seek to confirm these findings with a more exhaustive analysis that includes TPW and other relevant environmental variables. Furthermore, we will incorporate GMI 166 GHz observations to understand if the 166 GHz channel provides more a more distinctive scattering signature compared to 89 GHz for shallow convective snowfall events, thus providing additional information that can be used to improve radiometer snowfall retrievals. The 183 GHz channels will also be explored for shallow convective snow events, similar to the analysis provided in Fig. 4.

References

Behrangi, A., M. Christensen, M. Richardson, M. Lebsock, G. Stephens, G. J. Huffman, D. Bolvin, R. F. Adler, A. Gardner, B. Lambrigtsen, and E. Fetzer, 2016: Status of high-latitude precipitation estimates from observations and reanalyses. *J. Geophys. Res. Atmos.*, **121**, 4468-4486, doi: 10.1002/2015JD024546.

Bennartz R., and P. Bauer, 2003: Sensitivity of microwave radiances at 85–183 GHz to precipitating ice particles, *Radio Sci.*, **38 (4)**, 8075, doi:10.1029/2002RS002626.

Bennartz, R., and G. W. Petty, 2001: The sensitivity of microwave remote sensing observations of precipitation to ice particle size distributions. *J. Appl. Meteor.*, **40**, 345-364.

Boening, C., M. Lebsock, F. Landerer, and G. Stephens, 2012: Snowfall‑driven mass change on the East Antarctic ice sheet. *Geophys. Res. Lett.*, **39(21)**.

Casella, D., G. Panegrossi, P. Sanò, A. C. Marra, S. Dietrich, B. T. Johnson, and M. S. Kulie, 2017: Evaluation of the GPM-DPM snowfall detection capability: Comparison with CloudSat-CPR. *Atmos. Res.*, In Press.

Di Michele, S., and P. Bauer, 2006: Passive microwave radiometer channel selection based on cloud and precipitation information content. *Quart. J. Roy. Meteor. Soc.*, **132**, 1299–1323, doi:10.1256/qj.05.164.

Kongoli, C., P. Pellegrino, R. R. Ferraro, N. C. Grody, and H. Meng, 2003: A new snowfall detection algorithm over land using measurements from the Advanced Microwave Sounding Unit (AMSU). *Geophys. Res. Lett.*, **30**, 1756, doi:10.1029/2003GL017177.

Kongoli, C., H. Meng, J. Dong, and R. Ferraro, 2015: A snowfall detection algorithm over land utilizing high-frequency passive microwave measurements—Application to ATMS. *J. Geophys. Res. Atmos.*, **120**, 1918–1932, doi:10.1002/2014JD022427.

Kulie, M. S., and R. Bennartz, 2009: Utilizing spaceborne radars to retrieve dry snowfall. *J Appl Meteor Clim*, **48**, 2564-2580.

Kulie, M. S., R. Bennartz, T. J. Greenwald, Y. Chen, and F. Z. Weng, 2010: Uncertainties in microwave properties of frozen precipitation: Implications for remote sensing and data assimilation. *J Atmos Sci*, **67**, 3471-3487.

Kulie, M. S., 2016: A shallow cumuliform snowfall census using spaceborne radar. *J. Hydrometeor.*, **17**, 1261-1279. doi: 10.1175/JHM-D-15-0123.1

Kummerow, C. D., D. L. Randel, M. Kulie, N.-Y. Wang, R. Ferraro, S. J. Munchak, and V. Petkovic, 2015: The evolution of the Goddard Profiling Algorithm to a fully parametric scheme. *J. Atmos. Oceanic Technol.*, **32**, 2265–2280. doi: http://dx.doi.org/10.1175/JTECH-D-15-0039.1

Kuo, K., W.S. Olson, B.T. Johnson, M. Grecu, L. Tian, T.L. Clune, B.H. van Aartsen, A.J. Heymsfield, L. Liao, and R. Meneghini, 2016: The microwave radiative properties of falling snow derived from nonspherical ice particle models. Part I: An extensive database of simulated pristine crystals and aggregate particles and their scattering properties *J. Appl. Meteor. Climatol.,* **55**, 691–708, doi: 10.1175/JAMC-D-15-130.1.

Liu, G., 2008: Deriving snow cloud characteristics from CloudSat observations. *J. Geophys. Res.*, **113**, D00A09, doi:10.1029/ 2007JD009766.

Noh, Y.-J., G. Liu, A. S. Jones, and T. H. Vonder Haar, 2009: Toward snowfall retrieval over land by combining satellite and in situ measurements. *J. Geophys. Res*., **114**, D24205, doi:10.1029/2009JD012307.

Olson, W.S., L. Tian, M. Grecu, K. Kuo, B.T. Johnson, A.J. Heymsfield, A. Bansemer, G.M. Heymsfield, J.R. Wang, and R. Meneghini, 2016: The microwave radiative properties of falling snow derived from nonspherical ice particle models. Part II: Initial testing using radar, radiometer and in situ observations. *J. Appl. Meteor. Climatol.,* **55**, 709–722, doi: 10.1175/JAMC-D-15-0131.1

Petty, G. W., 1994: Physical retrievals of over-ocean rain rate from multichannel microwave imagery. Part 1: Theoretical characteristics of normalized polarization and scattering indexes. *Meteorology and Atmospheric Physics,* **54**, 79-99.

Prigent, C., F. Aires, and W. Rossow, 2006: Land surface microwave emissivities over the globe for a decade. *Bull. Amer. Meteor. Soc*., **87**, 1573–1584, doi:10.1175/BAMS-87-11-1573.

Skofronick-Jackson, G,M.-J. Kim, J. A. Weinman, and D.-E. Chang, 2004:A physical model to determine snowfall over land by microwave radiometry. *IEEE Trans. Geosci. Remote Sens*., **42**, 1047–1058, doi:10.1109/TGRS.2004.825585.

Skofronick-Jackson, G., and B. T. Johnson, 2011: Surface and atmospheric contributions to passive microwave brightness temperatures for falling snow events. *J. Geophys. Res*., **116**, D02213, doi:10.1029/2010JD014438.

Spencer, R.W., H.M. Goodman, and R.E. Hood, 1989: Precipitation retrieval over land and ocean with the SSM/I: Identification and characteristics of the scattering signal. *J. Atmos. Oceanic Technol.*, **6**, 254–273.

Surussavadee, C., and D. H. Staelin, 2009: Satellite retrievals of arctic and equatorial rain and snowfall rates using millimeter wavelengths. IEEE Trans. Geosci. Remote Sens., 47, 3697–3707, doi:10.1109/TGRS.2009.2029093.

Turk, F. J., Z. S. Haddad, and Y. You, 2014: Principal components of multifrequency microwave land surface emissivities. Part I: Estimation under clear and precipitating conditions. *J. Hydrometeor*., **15**, 3–19, doi:10.1175/JHM-D-13-08.1.

You, Y., N. Y. Wang, R. Ferraro, and S. Rudlosky, 2016: Quantifying the Snowfall Detection Performance of the GPM Microwave Imager Channels over Land. *J. Hydrometeor.*, 729-751, doi: 10.1175/JHM-D-16-0190.1.